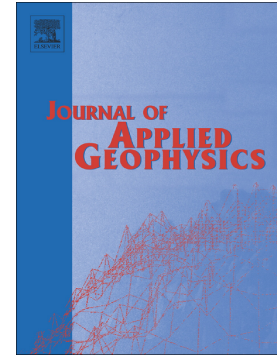


Inversion of multimodal dispersion curves from distributed acoustic sensing measurements for subsurface imaging: A field case of Garner Valley, California

Yingwei Yan, Xiaofei Chen, Jing Li, Jianbo Guan, Chaoqiang Xi, Hui Liu



PII: S0926-9851(23)00148-9

DOI: <https://doi.org/10.1016/j.jappgeo.2023.105070>

Reference: APPGEO 105070

To appear in: *Journal of Applied Geophysics*

Received date: 7 February 2023

Revised date: 11 April 2023

Accepted date: 18 May 2023

Please cite this article as: Y. Yan, X. Chen, J. Li, et al., Inversion of multimodal dispersion curves from distributed acoustic sensing measurements for subsurface imaging: A field case of Garner Valley, California, *Journal of Applied Geophysics* (2023), <https://doi.org/10.1016/j.jappgeo.2023.105070>

This is a PDF file of an article that has undergone enhancements after acceptance, such as the addition of a cover page and metadata, and formatting for readability, but it is not yet the definitive version of record. This version will undergo additional copyediting, typesetting and review before it is published in its final form, but we are providing this version to give early visibility of the article. Please note that, during the production process, errors may be discovered which could affect the content, and all legal disclaimers that apply to the journal pertain.

# Inversion of Multimodal Dispersion Curves from Distributed Acoustic Sensing Measurements for Subsurface Imaging: A field case of Garner Valley, California

Yingwei Yan<sup>a,\*</sup>, Xiaofei Chen<sup>b,c,\*</sup>, Jing Li<sup>d</sup>, Jianbo Guan<sup>e</sup>, Chaoqiang Xi<sup>f</sup> and Hui Liu<sup>d</sup>

<sup>a</sup> Department of Earth and Space Sciences, Southern University of Science and Technology, Shenzhen, China.

<sup>b</sup> Shenzhen Key Laboratory of Deep Offshore Oil and Gas Exploration Technology, Southern University of Science and Technology, Shenzhen, China.

<sup>c</sup> Guangdong Provincial Key Laboratory of Geophysical High-resolution Imaging Technology, Southern University of Science and Technology, Shenzhen, China.

<sup>d</sup> College of Geo-exploration Science and Technology, Jilin University, Changchun, China.

<sup>e</sup> School of Geological Engineering and Geomatics, Chang'an University, Xi'an, China.

<sup>f</sup> School of Earth and Environment, Anhui University of Science and Technology, Huainan, China.

## ABSTRACT

Utilizing the surface-wave (Rayleigh-wave) dispersion properties to estimate subsurface S-wave velocity structure has become a popular method due to simple data collection and analysis procedure during the past decades. In particular, the promotion of distributed acoustic sensing (DAS) technique enhances its popularity due to the low-cost of ultra-dense observations. Moreover, under the same exploration requirement, the cost of the DAS data collection is much lower than that of the traditional acquisition implemented by the nodal seismographs. Therefore, it is necessary to expand the DAS application. Here, the multimodal surface-wave dispersion curves are successfully extracted from the phase-weighted stack of cross-correlation functions (CCFs) of the DAS data collected at Garner Valley Downhole Array field site, California by the

proposed cylindrical-wave phase-shift. Then, the dispersion curves are inverted by the inversion workflow (expected to avoid the mode-misidentification) proposed by Yan et al. (2022a), consisting of staging strategy and pattern search with embedded Kuhn-Munkres (PSEKM) algorithm. Compared with other inversion schemes, the novel inversion method allows the presence of the observed values without prior mode-order definition in the inversion system, which omits the tedious and risky manual mode identification, and the mode-orders would be predicted dynamically during the inversion. The dispersion fittings for certain survey points indicate that the mode losses and aliasings appear to be widespread for the surface waves recorded on the free-surface. Finally, the S-wave velocity tomogram consistent with the geological materials of survey area is revealed. Our study demonstrates the feasibility of extracting the DAS-derived multimodal dispersion information and consequently obtaining a physical-reasonable subsurface S-wave velocity model.

## **Keywords:**

Surface waves; Distributed-acoustic Sensing; Dispersion inversion; Pattern search; Kuhn-Munkres algorithm

## **1. Introduction**

Subsurface S-wave velocity is one of the most important seismic parameters, which is related to the mechanical properties of the medium, and it is also seen as a vital indicator for evaluating the dynamic characteristics of the shallow-surface media (Yilmaz et al., 2006). Moreover, as Imai and Tonouchi (1982) proved, the S-wave velocity is also correlated with the stratum hardness index  $N$  of the soil mechanism and foundation engineering. In addition, it is also required for the following fields, such as the site classification (Fäh et al., 2003; Tan et al., 2012), reservoir characterization and fluid identification in unconventional resources (Guo and

Li, 2015), prediction of rock porosity (Uyanik, 2019), static correction of migration (Mari, 1984; Askari et al., 2015; Papadopoulou et al., 2020), and so on.

Nowadays, multi-channel analysis of surface waves (MASW) (Xia et al., 1999) utilizing the dispersion properties has become almost the most popular noninvasive method for revealing the layered S-wave velocity ( $V_s$ ) structure of underground media due to simple data collection and analysis procedure (Socco et al., 2010; Xia et al., 2015; Guan et al., 2022). Especially, the promotion of distributed acoustic sensing (DAS) technique extends the data collection method of MASW (Vantassel et al., 2022). DAS is a rapidly developing technique that utilizes the principle of coherent optical time-domain reflectometry to measure the spatial distribution of extensional strain or strain rate along an optical fiber (Parker et al., 2014), and each channel of the DAS data is equivalent to the integral of the spatial derivative of the particle displacement along the fiber axis (strain) within a certain distance, which is called gauge-length. There is a deterministic relationship between the strain recorded by DAS and displacement recorded by seismograph, therefore, the surface-wave (referring to the Rayleigh-wave) dispersion information can be extracted from the DAS data, which has been verified by Zeng et al. (2017). Furthermore, DAS can combine with the widespread dark fiber networks to proceed the imaging for subsurface structures (Dou et al., 2017; Jousset et al., 2018). Thus, the affordable, quick- and easy-to-deployment DAS stimulates the research interest of scholars and restores the vitality of the “dated” surface-wave imaging technique, till now, many  $V_s$  imaging cases using the DAS technique have been reported (Cheng et al., 2021, 2022; Lancelle et al., 2021; Liu et al., 2022; Song et al., 2020, 2021).

Currently, the common inversion strategies often limit the attention to the fundamental-mode dispersion curve (Lamuraglia, 2023), although many researchers have emphasized that the

higher-mode dispersion information is essential to better constrain the 1-D S-wave velocity solution (Xia et al., 2003; Ernst, 2008; Maraschini et al., 2010a; Maraschini and Foti, 2010b; Pan et al., 2019; Yan et al., 2022a). There may be two reasons for this phenomenon. The first reason is that the high-modal surface-wave components observed on the free-surface tend to be weak, which brings difficulties to the stable extraction. Another reason is the potential mode-misidentification caused by the mode-losses and aliasings, and the wrong identification for the order-labelling would bring a negative impact to the inversion (Yan et al., 2022a). Especially the mode-misidentification at the low frequency-band, which may introduce more than 50% errors to the inverted structure (O’Neil and Matsuoka, 2005). The double-edged sword characteristics of higher-mode surface-wave dispersion data may discourage many people, limiting the utilization of the multimodal dispersion, regardless of the traditional data or DAS data. To utilize the higher-mode dispersion data reliably, Maraschini and Foti (2010b) adopted a new misfit function based on the Haskell–Thomson matrix method, which allows higher modes to be taken into account without need to associate experimental data point to a specific mode. However, there are a large number of local minimum areas on the hyper-surface of the new misfit function, which is needed to optimize by global optimization algorithms (Maraschini and Foti, 2010b). Thus, the computation-scale of the inversion strategy proposed by Maraschini and Foti (2010b) is relatively large. We also construct a novel inversion workflow of the multimodal surface wave dispersion curves based on the ideas of stepwise refinement and optimal data matching (Yan et al., 2022a), recently, which consists of the staging strategy and pattern search (Conn et al., 1991) with embedded Kuhn-Munkres algorithm (PSEKM) (Kuhn, 1955; Munkres, 1957; West, 2020). This novel inversion method also allows the presence of the observed values without prior mode-order definition in the inversion system, and the mode-order labels would be predicted

dynamically during the inversion. The previously reported synthetic tests and field data cases have proved the effectiveness of the novel inversion method (Yan et al., 2022a), therefore, it is selected as the inversion method for the DAS-derived dispersion data in the article.

Reliable dispersion spectrum is the prerequisite for realizing the effective inversion of surface-wave dispersion curves. The calculation methods for the dispersion spectrum can be divided into two types, which are the plane-wave-based and cylindrical-wave-based methods. For example, the common linear Radon transform (McMechan and Yedlin, 1981), high-resolution linear Radon transform (Luo et al., 2008) and phase shift (Park et al., 1998) are the typical calculation methods for the dispersion spectrum based on the plane-wave propagation. However, the surface-wave in real world is excited by a point source, which is propagated by the form of cylindrical-wave. Therefore, the dispersion spectrum calculation methods based on the plane-wave would introduce the model incompatibility errors under some circumstances (Yan et al., 2022a). Compared with these plane-wave-based methods, the frequency-Bessel (F-J) transformation (Wang et al., 2019; Xi et al., 2021; Zhou and Chen, 2021) is a dispersion spectrum calculation method based on the cylindrical-wave propagation. The original F-J transformation is constructed for the dispersion extraction of traditional cross-correlation functions (CCFs) (extracted from the common seismic data, Wang et al., 2019), while the CCFs retrieved from the DAS data would be modulated in the frequency domain compared with the traditional CCFs (Vantassel et al., 2022). Therefore, the original F-J transformation may not be suitable for extracting the dispersion spectrum of DAS-derived CCFs. Considering this possible fact, we propose the cylindrical-wave phase-shift that does not rely on the frequency-domain amplitude of CCFs to calculate the dispersion spectrum. The specific derivations and formulae about the cylindrical-wave phase-shift are placed at the Section 2.1.

In the field DAS data application, we first retrieve the CCFs of the DAS data collected at Garner Valley Downhole Array (GVDA) field test site, California, and the phase-weighted stack (PWS) (Schimmel and Paulssen, 1997) is adopted to stack the segmented CCFs in this process to increase the abundance of information. The critical role of PWS for improving the quality of CCFs would be commented below. Then, we exploit the multimodal surface-wave dispersion information from the CCFs utilizing the cylindrical-wave phase-shift. Finally, the quasi-2D  $V_s$  tomogram that highly consistent with the geological materials of survey area is generated by adopting our inversion workflow. We hope that this research would serve as a demonstration of extracting and utilizing the DAS-derived multimodal dispersion information, construct a dedicated scheme for DAS data analysis, raise up the confidence in utilizing the multimodal/high-modal surface-wave dispersion in both DAS and nodal-seismograph application scenarios.

## 2. Method

### 2.1. Cylindrical-wave phase-shift

The particle displacement records excited by a point source can be regarded as the convolution of the source wavelet and the Green's function in the time domain, having a product relationship in the frequency domain, so the spectrum of the particle displacement  $u$  with the angular frequency  $\omega$  and the distance  $r$  from the source is expressed as:

$$u(\omega, r) = s(\omega)G(\omega, r) = |s(\omega)| |G(\omega, r)| \exp(i\Phi(k_\omega r) + i\theta_s) = |u(\omega, r)| \exp(i\Phi(k_\omega r) + i\theta_s), \quad (1)$$

where  $G$  represents the Green's function,  $k_\omega$  is the angular-wavenumber of surface waves with the form of  $\omega/v$ ,  $\omega$  and  $v$  are the angular frequency and phase velocity, respectively,  $i$  is the imaginary unit,  $\Phi$  denotes the phase angle related to  $k_\omega$  and  $r$ ,  $\Phi$  can be derived from the diffusion mechanism of surface waves, cylindrical or plane-wave propagation (Zywicki and Rix,

2005; Haney and Nakahara, 2014), and  $\theta_s$  is the initial phase of the source at the angular frequency  $\omega$ . Considering two recording points  $A$  and  $B$  with the distance  $r_A$  and  $r_B$  from the source, taking  $A$  as the reference (virtual source), the spectrum of the cross-correlation function (CCF) between  $A$  and  $B$  is:

$$\begin{cases} C_{AB}^u(\omega, \Delta r) = u(\omega, r_A)^* u(\omega, r_B) = |u(\omega, r_A)| |u(\omega, r_B)| \exp(i\Phi(k_\omega \Delta r)), \\ \Delta r = r_B - r_A, \end{cases} \quad (2)$$

where  $C_{AB}^u$  is the CCF, the symbol  $*$  represents the conjugate operation. The cross-correlation removes the initial phase of the source, thus we can calculate the dispersion spectrum  $E$  utilizing the real and imaginary part of the CCF, separately, which is.

$$\begin{aligned} E(\omega, k) &= \int \left[ \text{real} \left( \frac{C(\omega, r)}{|C(\omega, r)|} \right) \cos(\Phi^S(kr)) + i \text{imag} \left( \frac{C(\omega, r)}{|C(\omega, r)|} \right) \sin(\Phi^S(kr)) \right] dr, \\ &= \int \left[ \cos(\Phi(k_\omega r)) \cos(\Phi^S(kr)) + \sin(\Phi(k_\omega r)) \sin(\Phi^S(kr)) \right] dr, \\ &= \int \cos[\Phi(k_\omega r) - \Phi^S(kr)] \end{aligned} \quad (3)$$

$\Phi^S$  is the scanned phase angle function related to the trial angular wavenumber  $k$  and the distance  $r$  to the virtual source. When  $\Phi^S$  equals to  $\Phi$ , the integrand function reaches the maximum value, and the peaks would occur on the dispersion spectrum, thus realizing the phase velocity measurement for surface waves. The DAS measurement is different from that of the classical nodal seismometer, and its record is the integral of the spatial derivative of the  $R$ -component displacement (strain) over the gauge-length (Vantassel et al., 2022). Therefore, its frequency-domain signal at  $\omega$  with the distance  $r$  from the source is:

$$\begin{aligned} DAS(\omega, r) &= \frac{1}{l} \int_{r-0.5l}^{r+0.5l} \frac{\partial u(\omega, r)}{\partial r} dr = \frac{1}{l} [u(\omega, r+0.5l) - u(\omega, r-0.5l)], \\ &\approx \frac{|u(\omega, r)|}{l} \left[ \exp(i(\Phi(k_\omega r + 0.5k_\omega l) + \theta_s)) - \exp(i(\Phi(k_\omega r - 0.5k_\omega l) + \theta_s)) \right]. \end{aligned} \quad (4)$$



In the above formula,  $l$  represents the gauge-length. Likewise, let the point  $A$  be the virtual source, and the CCF of the DAS records between point  $A$  and  $B$  is as follows:

$$\left\{ \begin{array}{l} C_{AB}^{DAS}(\omega, \Delta r) = DAS(\omega, r_A)^* DAS(\omega, r_B) = \frac{2}{(l)^2} [1 - \cos \Phi(k_\omega l)] C_{AB}^u(\omega, \Delta r), \\ \quad \quad \quad = \frac{2}{(l)^2} P(k_\omega l) C_{AB}^u(\omega, \Delta r), \\ \Delta r = r_B - r_A. \end{array} \right. \quad (5)$$

Compared the CCF derived from the displacement records, there is an amplitude modulation term  $P$  in the retrieved  $RR$ -component CCF for the DAS records. There are two forms to define the phase angle  $\Phi$  for the DAS data, which are:

$$\left\{ \begin{array}{l} \Phi(k_\omega r) = \arctan \left( \frac{Y_2(k_\omega r) - Y_0(k_\omega r)}{J_0(k_\omega r) - J_2(k_\omega r)} \right) \quad \text{cylindrical-wave,} \\ \Phi(k_\omega r) = -k_\omega r + \frac{1}{4}\pi \quad \text{plane-wave,} \end{array} \right. \quad (6)$$

where  $J_0$  and  $J_2$  are the 0-order and 2-order Bessel functions of the first kind, and  $Y_0$  and  $Y_2$  represent the 0-order and 2-order Bessel functions of the second kind. The cylindrical-wave phase angle in the first row of formula (6) is determined according to the research of Haney and Nakahara (2014). The plane-wave phase angle in the second row is derived from the asymptotic properties of the Bessel function when the argument is infinite. The cylindrical-wave phase is more general than the plane-wave phase, especially for the near-field dispersion measurement, while the plane-wave phase is only suitable for the far-field conditions. It is necessary to point out that in the above deduction process, the operator of the Fourier transform is  $e^{-i\omega t}$ . Also, there are two forms about the definition for  $P$ , which are:

$$\begin{cases} P = 1 - \cos \left( \arctan \left( \frac{Y_2 \left( \frac{2\pi l}{\lambda} \right) - Y_0 \left( \frac{2\pi l}{\lambda} \right)}{J_0 \left( \frac{2\pi l}{\lambda} \right) - J_2 \left( \frac{2\pi l}{\lambda} \right)} \right) \right) & \text{cylindrical-wave,} \\ P = 1 - \cos \left( -\frac{2\pi l}{\lambda} + \frac{1}{4} \pi \right) & \text{plane-wave.} \end{cases} \quad (7)$$

$\lambda$  represents the wavelength of surface waves, and Fig. 1 shows the amplitude modulation term  $P$  as a function of the ratio between  $\lambda$  and  $l$  for the cylindrical and plane-wave diffusion mechanisms, respectively. The shapes of the two  $P$ -value curves are similar with only slight amplitude differences (Figs. 1 (a) and (b)). When the ratio between  $\lambda$  and  $l$  is less than 1, the zero-points appear in the  $P$ -value curves, and the closer to 0, the denser the zero-points and the pole-points (Figs. 1 (a) and (b)), making the curves more oscillating, which would greatly degrade the amplitude of DAS data for measuring the wavelengths smaller than the gauge-length. Vantassel et al. (2022) also indicated that the wavelengths shorter than one gauge-length cannot be measured reliably in practice. Therefore, with a conservative attitude, we set the smallest measurable wavelength for the DAS data in the article as one gauge-length. Different phase angle functions in formula (3) define different phase-shift methods, which would be specialized as the cylindrical-wave phase-shift when the cylindrical-wave phase is adopted. For the dispersion measurement in the article, we use the cylindrical-wave phase-shift to extract the dispersion spectrum from the CCFs.

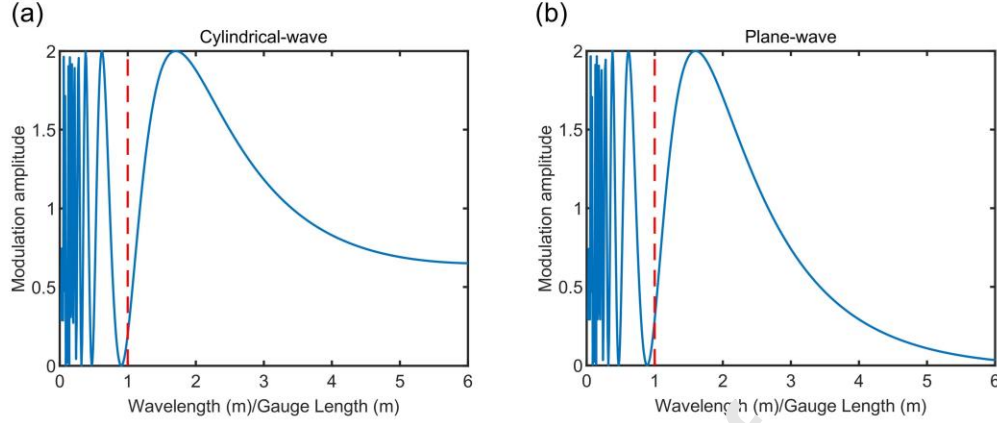


**Fig. 1.** The amplitude modulation term  $P$ -value curves for the DAS data of different surface wave diffusion mechanisms, cylindrical-wave (a) and plane-wave (b) propagation. The points of the red dashed lines in (a) and (b) satisfy that the wavelength divided by the gauge-length equals to 1.

## 2.2. Revisit the staging strategy and PSEKM

Here, we would briefly introduce the concept and operation of the proposed inversion method, and the specific formulae and implementation about it can be found in our previous published article (Yan et al., 2022b). The technical flowchart for the inversion method is given by Fig. 2, which can be summarized as:

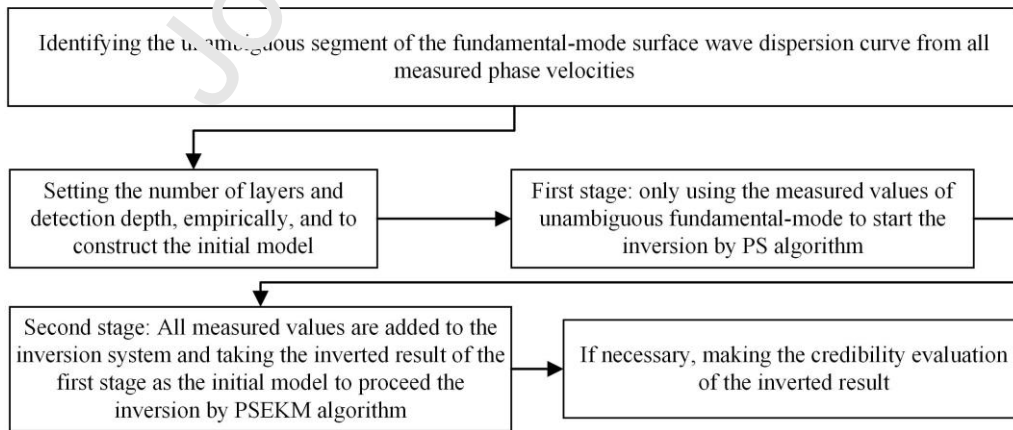


**Fig. 2.** The technical flowchart for the inversion method used in the article.

1) First stage: a) Constructing the initial model from the identified unambiguous segment of the fundamental-mode surface wave dispersion curve (Yan et al., 2022a); b) Using the pattern search (PS) (Conn et al., 1991; Song et al., 2009) to invert the identified fundamental-mode dispersion observations to get the inverted S-wave velocity structure.

2) Second stage: Adding all dispersion observations to the inversion system, the inversion result of the first stage is set as the initial model for the second-stage inversion, and the mode-orders of the measured phase velocities with no-explicitly-specified-mode-order (NESMO) would be dynamically evaluated for each model  $\mathbf{m}$  occurred in the iterative process. It is to build a weighted bipartite graph between the observed values with NESMO and predicted phase velocities (if the fundamental-mode observation is existent, representing the predicted values excluding the fundamental-mode, otherwise it's all). At each frequency, the weights of the edges are calculated by the negative distance based on the  $L^p$  norm ( $p$  is set as 2 in the paper), and a schematic bipartite graph  $G$  is shown by Fig. 3. Then, using the Kuhn-Munkres (KM) (Kuhn 1955; Munkres 1957; West 2020) to get the maximum matching of graph  $G$ , and the mode-orders of the observations with NESMO could be inferred from the matching relationship. That's to say, for each model  $\mathbf{m}$  that appears in the inversion process, its optimal allocation scheme for the dispersion observations with NESMO at each frequency is given by the KM algorithm (the optimal match between the predicted values of the current model  $\mathbf{m}$  and observations would be achieved because of this operation), then continuously updating the model parameters through the PS to make the misfit value smaller, so as to obtain a satisfactory inversion result.

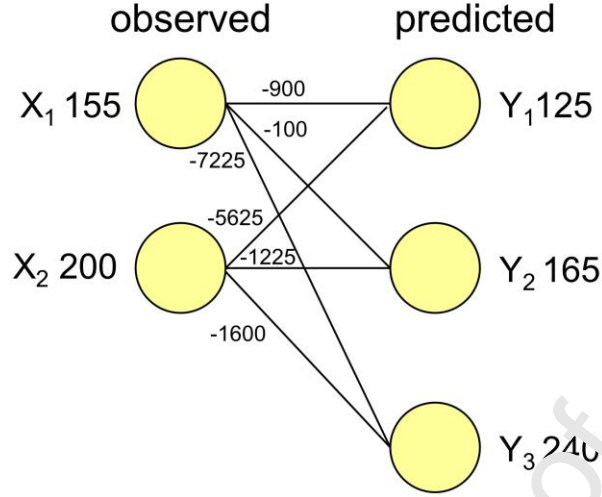


**Fig. 3.** A schematic weighted bipartite graph  $G$ , and the yellow solid circles denote the vertices. The vertices of the observed values with NESMO and the used predicted values at each frequency are represented by the sets  $X$  and  $Y$ , respectively. The numbers near the yellow solid circles represent the corresponding phase velocities, connecting the vertices of the observed values to all the used predicted values at a certain frequency to build the bipartite graph  $G$ . The weights of the edges of the bipartite graph  $G$  are derived by the negative distance based on the  $L^p$  ( $p$  is set as 2 in the paper) norm between the vertices of  $X$  and  $Y$ . The numbers on each edge represent the corresponding weight. The optimal match relationship for  $G$  is the vertex  $X_1$  matches  $Y_2$  and the vertex  $X_2$  matches  $Y_3$ , which defines the mode-order match relationship between the observed and predicted phase velocities. The optimal match relationships of all bipartite graphs of the inversion process would be automatically solved by the Kuhn-Munkres algorithm.

### 2.3. Credibility evaluation

How to evaluate the quality of the inversion result has always been a hot spot for geophysical inversion, here, we provide a semi-quantitative approach to assess the reliability of

the inversion from a probabilistic perspective. The a posteriori probability (probability density function)  $\sigma(\mathbf{m})$  for a model  $\mathbf{m}$  can be calculated as (Mosegaard and Tarantola, 1995):

$$\sigma(\mathbf{m}) = k_1 \rho(\mathbf{m}) L(\mathbf{m}), \quad (8)$$

where  $\rho(\mathbf{m})$  is the a priori probability for the model space, and all models in the model space are considered to have the same  $\rho$  value in this paper;  $k_1$  is a normalization constant, and the likelihood function  $L(\mathbf{m})$  is derived from the misfit function  $S(\mathbf{m})$ , which is related to the distance between the observed and predicted data, and reflecting the likelihood of a model  $\mathbf{m}$  appearing, as:

$$L(\mathbf{m}) = k_2 \exp(-S(\mathbf{m})), \quad (9)$$

$k_2$  is also a normalization constant. Then, the 1D conditional probability function of the inversion parameter at the  $j$ -th dimension is determined as.

$$\sigma(m_j^S | \mathbf{m}^{inv} \setminus m_j) = \frac{\sigma(m_j^S, \mathbf{m}^{inv} \setminus m_j)}{\sigma(\mathbf{m}^{inv} \setminus m_j)}, \quad (10)$$

where  $\mathbf{m}^{inv}$  represents the inverted result,  $m_j$  is the inversion parameter at the  $j$ -th dimension and  $m_j^S$  represents a sample within the searching range of the  $j$ -th dimensional parameter, the symbol  $\setminus$  denotes the subtraction operation. The denominator  $\sigma(\mathbf{m}^{inv} \setminus m_j)$  is considered to be a constant, also assuming that the following equation holds:

$$\int_{a_j}^{b_j} \sigma(m_j^S | \mathbf{m}^{inv} \setminus m_j) dm_j^S = 1. \quad (11)$$

In the above equation,  $a_j$  and  $b_j$  represent the lower and upper bound of the searching range of the  $j$ -th dimension, respectively. Equation (11) means that the  $j$ -th dimensional inversion parameter can only appear in the searching range we pre-determined, thus combining equation (10) and (11), we can calculate all 1D conditional probability density distributions (CPDDs) of the

inversion parameter at each dimension (Song et al., 2020). Please note the uniform sampling method is adopted for the calculation of the 1D CPDDs.

### 3. Field case

#### 3.1. Data acquisition and analysis workflow

The DAS data sets are collected at the GVDA field test site in Southern California in September 2013, and the survey area is adjacent to Highway 74 of California (Fig. 4 (a)). There are about 762 m of fiber-optic cable deployed for this area, and these cables are buried in the trenches with a depth of 15~46 cm in a rectangular design with two interior diagonal segments (Fig. 4 (a)). A stationary 45 kN mass shaker at the left of Long line I is chosen as the source (denoted by the red pentagram in Fig. 4 (a)), sweeping from direct current (DC) to 10 Hz and back to DC. The DAS data of Long line I induced by the sweep-frequency source is mainly distributed at the time interval of about 20~75 s, and the traffic noise part is distributed at the beginning and end part of the records (Fig. 4 (b)). The DAS strain rate has been downsampled to 200 Hz, for the spatial domain, the response is sampled in channel-spacing at 1 m with the gauge-length of 10 m (Lancelle et al., 2021). The spectrums of the DAS channels show that the most of the energy of the signals is distributed between 5~15 Hz (Fig. 4 (c)), presenting a challenge for us to accurately measure the surface-wave phase velocities at other frequencies. For this open DAS data, Lord et al. (2016) realized the phase measurement of fundamental-mode surface-wave at about 2~16 Hz by source-synchronous filter, Lancelle et al. (2021) also successfully extracted that information at 2 to 10 Hz using MASW and inverted a 1D S-wave velocity profile with the maximum penetration depth at about 30 m. Recently, Liu et al. (2022) gave the similar fundamental-mode dispersion measurement using the CCFs of DAS data and delineated a 2D S-wave velocity tomogram for the Long line I at depth above 25 m by inverting

the CCFs, directly. So far, the dispersion measurement and application about the higher-mode or multimodal surface waves for this DAS data have never been published. One possible reason is that the PWS technique is ignored for these researches, and the role of PWS for dispersion extraction would be shown in the following parts.

To avoid the effect of the off-line source on the phase velocity measurement, we only analyze the DAS datasets of Long line I. The complete analysis workflow is given by Fig. 4 (d), which can be roughly divided into three steps:

**Step 1, Dispersion measurement:** The data is segmented so that each segment has 5 s time-length with 80% overlap of adjacent segments. The segmented datasets are divided into a series of sub-windows along the spatial axis with each one consisting of 60 continuous channels, and moving the sub-window to the right with 1 m interval. Subsequently, for each sub-window, taking the first channel as the reference (virtual source), then there would be 125 CCFs gathers after the operation. In the process of extracting CCFs gather, the PWS is used to stack the segmented CCFs to improve the signal-to-noise ratio. The pre-processing steps for each segment have been abandoned in the flow to avoid the potential adverse effect, as the green fonts described in Fig. 4 (d). The inversion result of the corresponding sub-window is placed at the midpoint of its CCFs gather. Finally, calculating the dispersion spectrum from the causal part of each CCF gather (Fig. 5) by utilizing the cylindrical-wave phase-shift and picking the measured phase velocities of multimodal surface waves from the dispersion image according to the peaks.

**Step 2, Inversion of surface-wave dispersion curves:** Following the staging strategy and PSEKM (Yan et al. 2022a) to proceed the inversion of surface-wave dispersion curves. Please note that, unlike the thin layer strategy Xia et al. (1999) adopted, the S-wave velocity and



thickness of each layer are updated simultaneously, the ratio for P-wave velocity and S-wave velocity is taken as 3.0, and the density parameters are fixed at  $2000 \text{ kg/m}^3$  in the article.

**Step 3, Credibility evaluation:** The 1D CPDDs of the inverted result are calculated to semi-quantitatively evaluate the reliability of the inversion parameter at each dimension (Song et al. 2020).

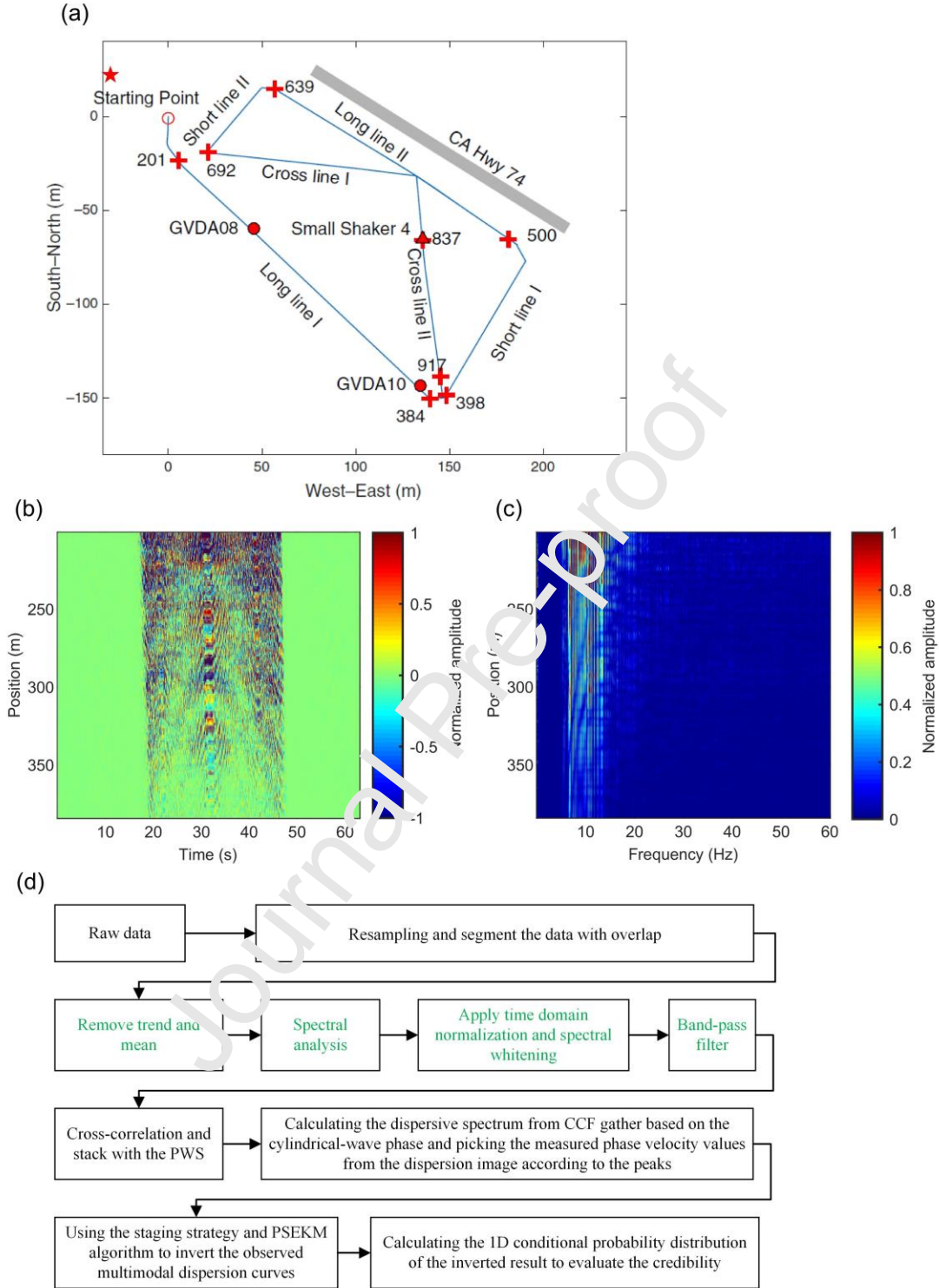


**Fig. 4.** The schematic map of the DAS survey, time-frequency characteristics of the data and dedicated workflow for the DAS data analysis. (a) A schematic map of the DAS fiber-optic cable

and location of the GVDA survey site (Zeng et al., 2017). The numbers (red crosses) denote the indexes of the DAS channels, please note the index does not start from 1. The red circles and solid triangle represent the seismic accelerometers and small vertical shaker, respectively. The red pentagram indicates the approximate location of the swept-frequency seismic source. (b) The DAS data of the Long line I and the amplitude has been globally normalized. (c) The amplitude spectra in the frequency-domain of the corresponding DAS channel in (b) with global normalization. (d) The analysis workflow for the field DAS data. The operations described with green fonts are not taken for the entire data analysis, although Bensen et al. (2007) have recommended these actions.

### 3.2. Inversion of surface-wave dispersion curves and credibility evaluation

Fig. 5 shows the CCFs of the entire Long line I with the first channel as the virtual source, and the causal parts occupy almost all the energy, indicating the unidirectional sources, even the traffic noise part. Therefore, only the causal part of the CCFs for the corresponding sub-window are used to calculate the dispersion spectrum. Fig. 6 gives the detailed displays of dispersion measurement and inversion for the 8-th sub-window. On the whole, the main events of the CCFs gather defined by the linear-stack (LS) and PWS are almost identical (Fig. 6 (a)). However, the waveform comparison of the single CCF at offset 30 m shows that there are spurious coda waves in the result of LS compared with that of PWS (Fig. 6 (b)), which are essentially a manifestation of high-frequency incoherent noise in the data, because the LS has no coherence measurement capability between these CCF segments. Thus, the dispersion observations at the high frequency-band are not reflected in the dispersion spectrum of the CCFs defined by the LS (Fig. 6 (c)), while that of the PWS can provide the extra higher-mode measurement at the high frequency-band (Fig. 6 (d)), and the comparisons for other sub-windows also show the identical behaviors

(Fig. 7). The additional dispersion observations are crucial, which would reduce the multi-solution of the inversion and reveal more truth about the subsurface media. It can be noticed that almost no considerable energy appears to the right of the black dashed lines (Figs. 6 (c) and (d)), reflecting the possible oscillation effect generated by the DAS system at this wavelength range. Therefore, with a conservative attitude, the smallest measurable wavelength for each sub-window is set as one gauge-length in the article. It is noted that the dispersion trend at the low-frequency band is still nice (Fig. 6 (d)), therefore, we rationally broaden the upper bound of the maximum measurable wavelength to 4 times of the spatial length of the corresponding sub-window. The upper bound for the maximum wavelength is not attained for all sub-windows, which is between 1.5 and 4 times of the spatial length, due to different dispersion quality. According to Occam's razor, we must choose the simplest one among the models that can fit the known dispersion observations (Yan et al., 2022b). Therefore, the initial model of each sub-window is constructed as a half-space model with 6-layer structure, empirically, and the S-wave velocity and layer thickness ( $h$ ) parameters are derived from the unambiguous fundamental-mode surface-wave dispersion curve (Yan et al., 2022a). The dispersion observations have been almost perfectly fitted and the predicted values of the second-stage inversion result indicate that the potential mode-losses and aliasings (Fig. 6 (d)). The mode-losses and aliasings appear to be widespread for the surface-wave observed at the free-surface (Fig. 8), and this is also the original motivation of adopting the novel inversion workflow. The initial misfit value at the second stage is slightly larger than the final misfit value of the first stage (Fig. 6 (e)), illustrating that the higher-mode surface-wave observations store the extra information about the subsurface structure, and this feature is more remarkable for certain sub-windows (Fig. 8 (c)). The inverted S-wave velocity structure of the first and second stage show the same increasing trend, but for

certain layers, the differences of  $V_S$  and  $h$  are obvious (Fig. 6 (f)), showing that the additional sensitivity of the higher-mode surface-wave observations to certain layers. To evaluate the inversion result, here, the  $V_S$  structure of nearby site (close to the parking lot; Stokoe et al., 2004) determined by the spectral-analysis-of-surface waves (SASW) at 2004 is given (Fig. 6 (f)). The inversion result of the second stage and that determined by the SASW have the same incremental structure below the depth of about 18 m, which verifies the reliability (Fig. 6 (f)). There are inconsistencies between the two results at depth above about 18 m (Fig. 6 (f)), the existing materials indicate the jumps of the result of the SASW is caused by the surface gravel (Stokoe et al., 2004). However, there is almost no gravel on the surface of our survey area, thus the differences above the depth of 18 m just reflect the credibility of the inversion result. The detection depth of the SASW is only about 25 m because of the lack of the low-frequency dispersion information, and its half-space S-wave velocity is about the average value of our result at this depth range (Fig. 6 (f)). In other words, our result realizes a finer description for this depth range due to the participation of the lower-frequency and high-modal dispersion observations in the inversion system.

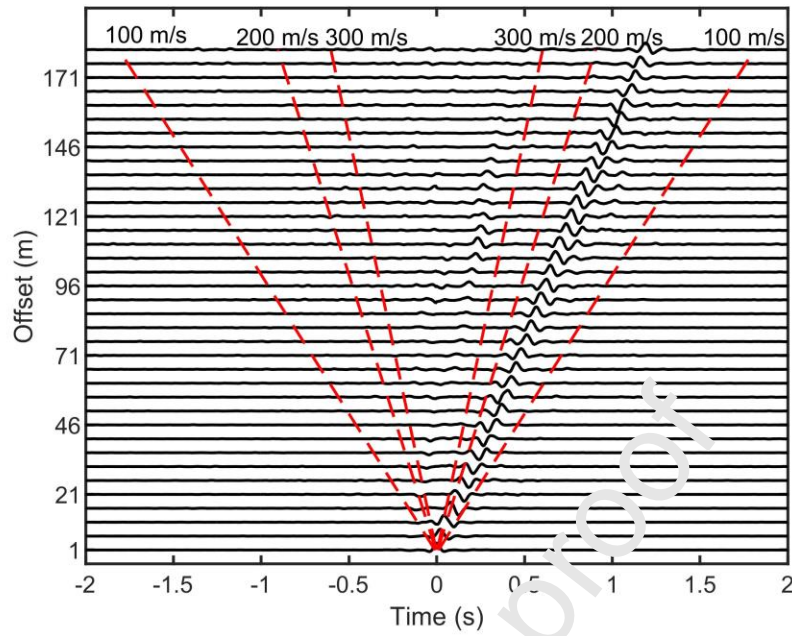


**Fig. 5.** The CCFs gather for the whole Long line J with the first channel as the virtual source. The amplitude of each CCF is normalized to 0.5 according to the maximum absolute amplitude, and the channel-spacing is also adjusted to 5 m for clear waveform representation. The red dotted lines denote the reference lines with different apparent velocities.

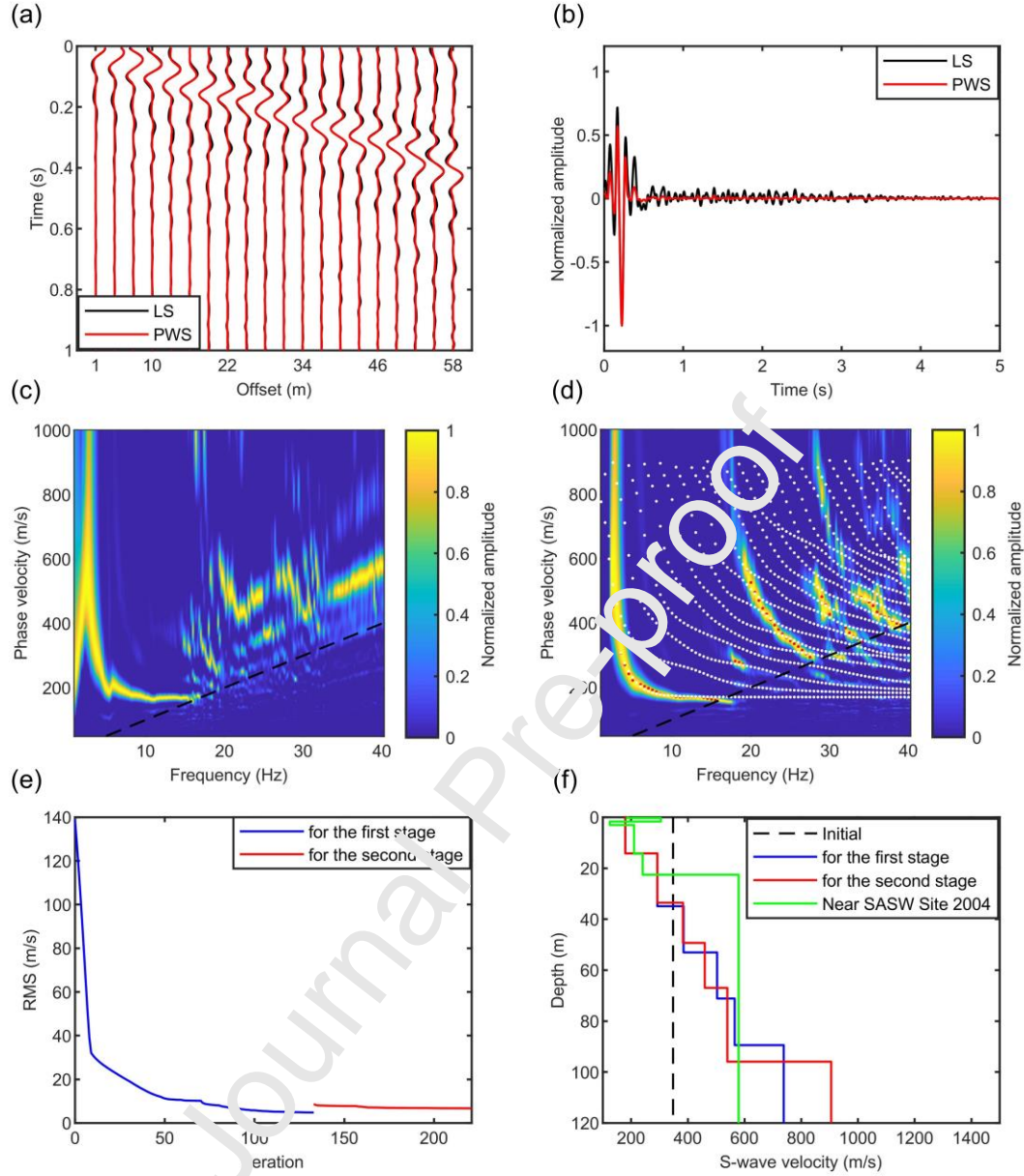


**Fig. 6.** The detail results of the dispersion measurement and inversion for the 8-th sub-window.

(a) The red and black waveforms are the CCFs defined by the phase-weighted stack (PWS) and linear stack (LS) (the midpoint of the CCFs gather is at the position of 238 m), respectively. For clarity, only the waveforms within 1 s with the channel-spacing at 3 m are shown, and the amplitude of each CCF is normalized to 0.5 according to the maximum absolute amplitude. (b) The detailed comparison of the normalized CCFs at offset 30 m obtained by the PWS and LS. (c)

The dispersion spectrum of the CCFs defined by the LS, which is extracted by the cylindrical-wave phase-shift. (d) The dispersion spectrum extracted from the CCFs defined by PWS by utilizing the cylindrical-wave phase-shift, the white and red dots denote the predicted phase velocities calculated from the inversion result at the second stage and observed phase velocities, respectively. (e) The descent curves for the misfit values (it is defined by the root-mean-square (RMS) error between the observed and predicted datasets) of the first and second stage. (f) The comparison for the initial, inverted S-wave velocity structure of the first and second stage, and S-wave velocity structure at nearby SASW site reported by Stokoe et al. (2004). The black dashed lines in (a) and (b) are defined by the gauge-length of the LAS data.



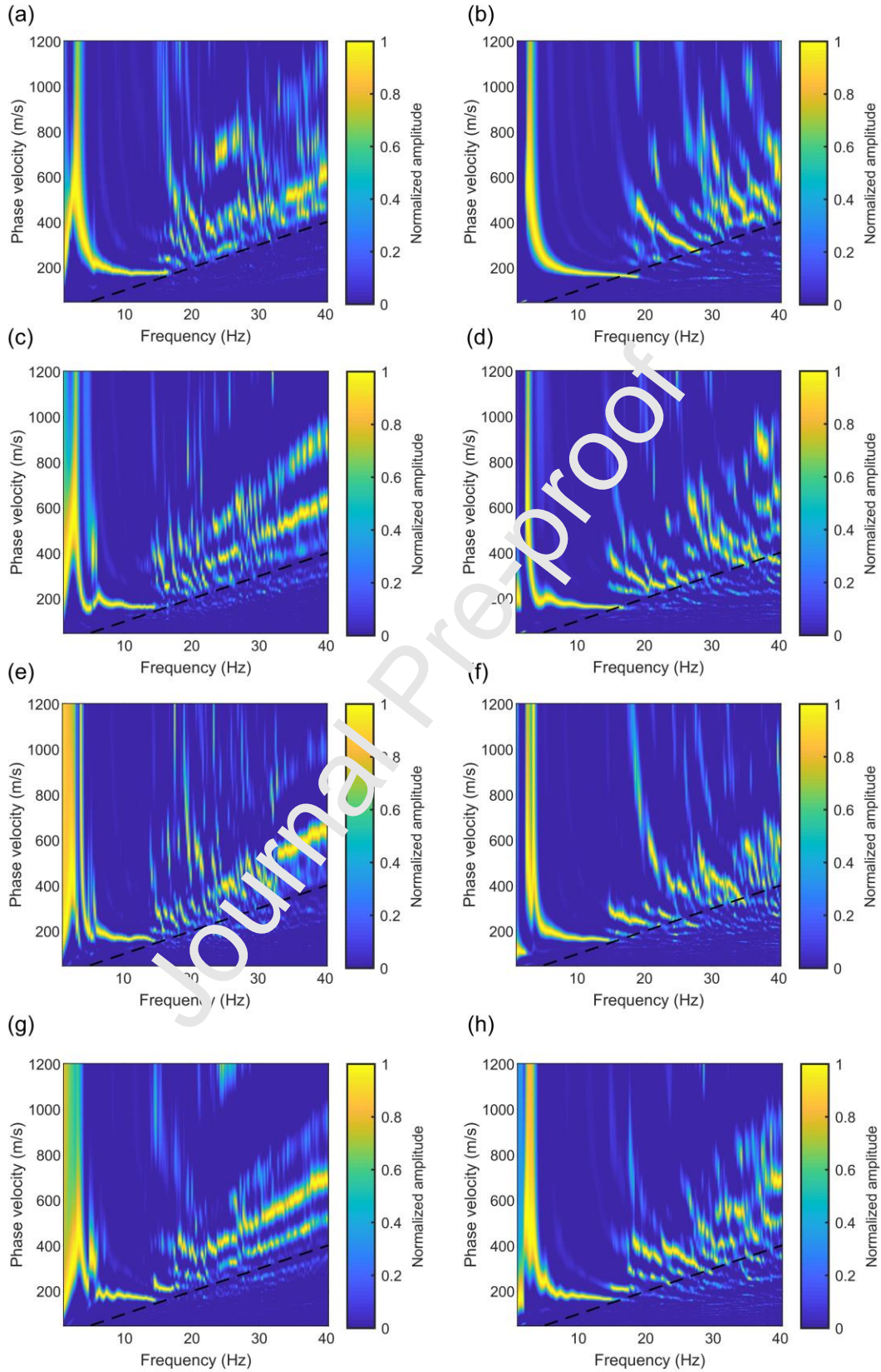


**Fig. 7.** The comparisons of the dispersion spectra extracted from the CCFs defined by the linear stack (LS) and phase-weighted stack (PWS) for certain sub-windows. All the dispersion spectra in the figure are calculated using the cylindrical-wave phase-shift. (a), (c), (e) and (g) are the dispersion spectra of the 1-st, 40-th, 80-th and 125-th sub-window, and the CCFs used are defined by the LS. (b), (d), (f) and (h) are also the dispersion spectra of those sub-windows, but the CCFs used are defined by the PWS. The black dashed lines in the above sub-figures are defined by the gauge-length of the distributed-acoustic-sensing (DAS) data.

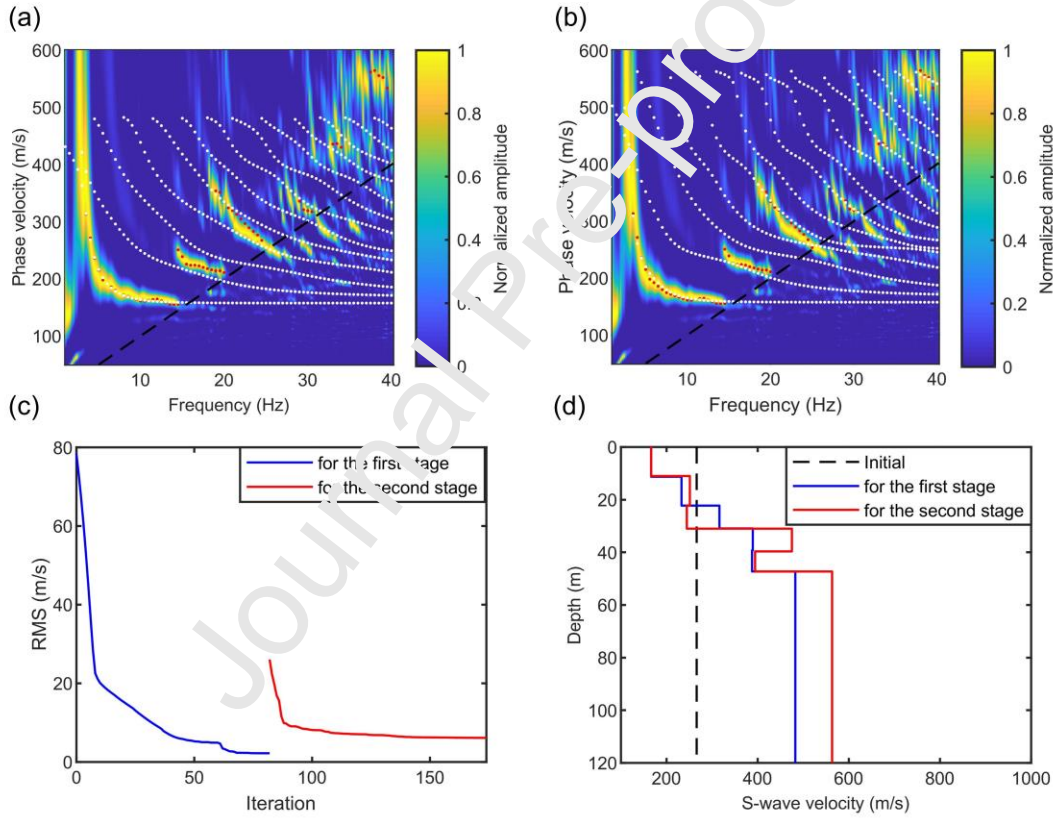


**Fig. 8.** The detail displays of the inversion of the surface-wave dispersion curves for the 102-nd sub-window. (a) The dispersion spectrum extracted from the CCFs defined by PWS by utilizing the cylindrical-wave phase-shift, the white and red dots denote the predicted phase velocities calculated from the inversion result at the first stage and observed phase velocities, respectively.

(b) is similar to (a), but the predicted phase velocities belong to the inversion result at the second stage. (c) The descent curves of the misfit values for these two stages, and the misfit function is defined by the root-mean-square (RMS) error between the observed and predicted datasets. (d) The comparison for the initial, inverted S-wave velocity structure of the first and second stage. The left regions of the black dashed lines in (a) and (b) define a reliable area for picking the measured phase velocities, and the points on the line satisfy the phase velocities divided by the frequencies equal to the gauge-length of the DAS data.

When there is no prior geological information or independent third-party geophysical materials about the survey area, how to evaluate the quality of the inversion result semi-quantitatively or quantitatively? We refer to the practice of Song et al. (2020), giving the 1D CPDDs of the inverted result for the 8-th sub-window, as shown by Fig. 9. The width of the 1D CPDD of different dimensions is different (Fig. 9), which reflects the different parameter sensitivities at different dimensions of the inversion system. The inversion parameter for each dimension can always exactly correspond to the peak of its 1D CPDD (Fig. 9), which indicates that the second-stage inversion has reached a strict global/local minimum point, and the same for other sub-windows (Fig. 10). Considering that the RMS error between the observed and predicted datasets of the 8-th sub-window is only 6.75 m/s, what's more the measurement errors are unavoidable. Thus, the strict global minimum point is likely to reach for the 8-th sub-window. Except for the 1D CPDD of the half-space S-wave velocity and layer thickness of fifth layer, the 1D CPDDs of the other inversion parameters are quite tight, showing the narrow confidence intervals and strong sensitivities for these parameters (Fig. 9). It can be observed that the 1D CPDDs of certain dimensions (the S-wave velocity of the fifth layer, and the thickness of the fourth and fifth layer) are not single-peaked (Fig. 10), which reflects the inherent ill-

conditioning of the inversion system belonging to the 102-nd sub-window. In other words, the parameters of these dimensions have stronger multi-solution compared with that of other dimensions because of the insufficient observation (although the partial higher-mode dispersion is utilized), which may cause the inappropriate parameter estimations for these dimensions. The inherent ill-conditioning of the inversion system of the 102-nd sub-window can only be reduced by enriching the observed values, while it is difficult to solve by selecting different inversion strategies.

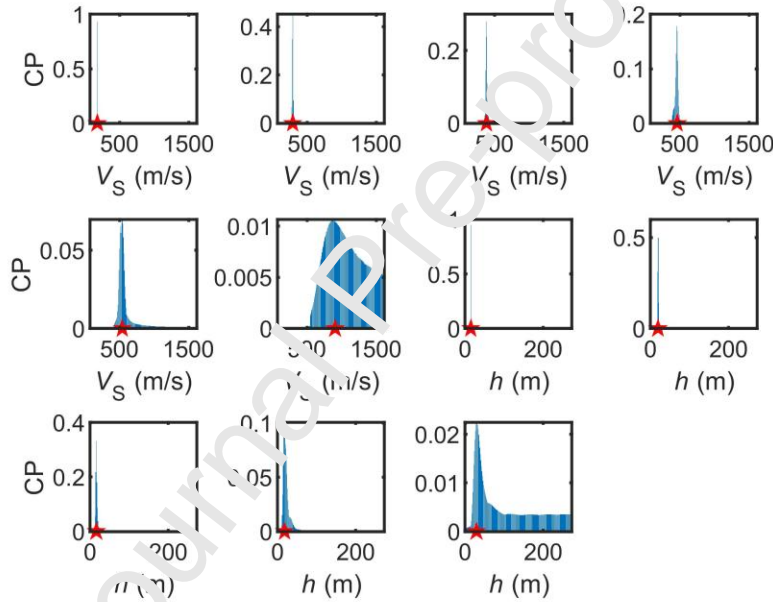


**Fig. 9.** Credibility evaluation for the inversion result at the second stage of the 8-th sub-window.

The 4 subgraphs of the first row represent the 1D CPDDs of the S-wave velocity parameter for first to fourth layers, the first two sub-images from the left in the second row are the 1D CPDDs of the S-wave velocity parameter for the 5-th and 6-th layers, the other two denote the 1D CPDDs of the thickness parameter of the first and second layer, and the sub-figures in the third row from left to right are the 1D CPDDs for the thickness parameter of the 3-rd to 5-th layer. The red pentagrams mark the inversion parameter of the corresponding dimension, and the range of

the horizontal axis of each subgraph is consistent with the searching range of the corresponding dimensional inversion parameter.

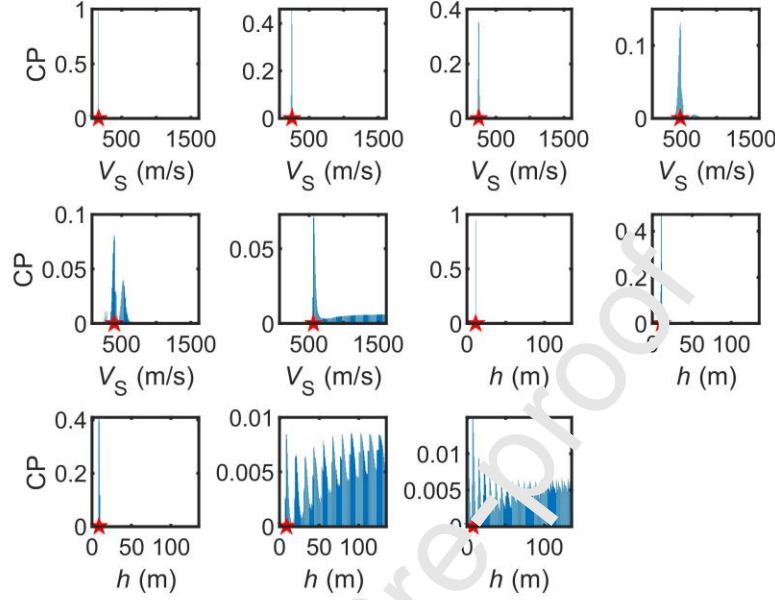


**Fig. 10.** The 1D CPDDs of the inversion result at the second stage for the 102-nd sub-window. The definition of the subgraphs is the same as that of the subgraphs of Fig. 9. The red pentagrams mark the inversion parameter of the corresponding dimension, and the range of the horizontal axis of each subgraph is consistent with the searching range of the corresponding dimensional inversion parameter.

To provide the critical evidence for evaluating the inversion results, we synthesize the  $R$ -component displacement records of the 8-th and 102-nd sub-windows with the discrete wavenumber method (Bouchon, 2003; Kausel, 2018; Zhang et al., 2020), and the source is placed on the free-surface. Then, we derive the corresponding DAS data following the formula (4), and extracting the CCFs and dispersion spectra (Fig. 11). For the 8-th sub-window, the observed CCFs are well fitted by the predicted CCFs, only there are very small discrepancies occurred at the surface-wave travelling-time for far offset CCFs (Fig. 11(a)). Furthermore, the

measured multimodal dispersion curves can be reflected in the dispersion spectrum extracted from the predicted CCFs of the 8-th sub-window, but the dispersion energy of the higher-mode surface-waves is relatively weak compared with that of the measured dispersion spectrum (Fig. 6 (d) and Fig. 11 (b)). For the 102-nd sub-window, the observed CCFs can still be properly fitted by the predicted CCFs (Fig. 11 (c)). The measured phase velocities of the fundamental-mode surface-wave are well reflected in the dispersion spectrum, and the considerable dispersion energy does not appear at the location for the ‘first’ and ‘second’ high-mode surface-wave observations (here, count the mode-order, visually; Fig. 11 (d)). The other high-mode observations may be manifested in the dispersion spectrum (Fig. 11 (d)). The discrepancies about the ‘first’ and ‘second’ high-mode surface-wave observations may be caused by the suppression effect of the fundamental-mode surface-wave, compared with the measured dispersion spectrum, the synthetic dispersion energy of the fundamental-mode surface-wave is excessive continuous (Fig. 6 (d), Fig. 8 (b), Figs. 11 (b) and (d)). Essentially, the excessive continuous dispersion energy of the fundamental-mode surface-wave indicates the inaccuracy of the current synthesis method of DAS data. Certainly, the inaccurate source mechanisms and the model-incompatibility between the theory and reality (such as the attenuation factor and lateral heterogeneity of the media are not considered) may also be the source of the differences between the observed and synthetic data. Overall, the appropriate CCFs fittings are realized for the 8-th and 102-nd sub-windows, which manifest the credibility and dependability of the corresponding inversion result.



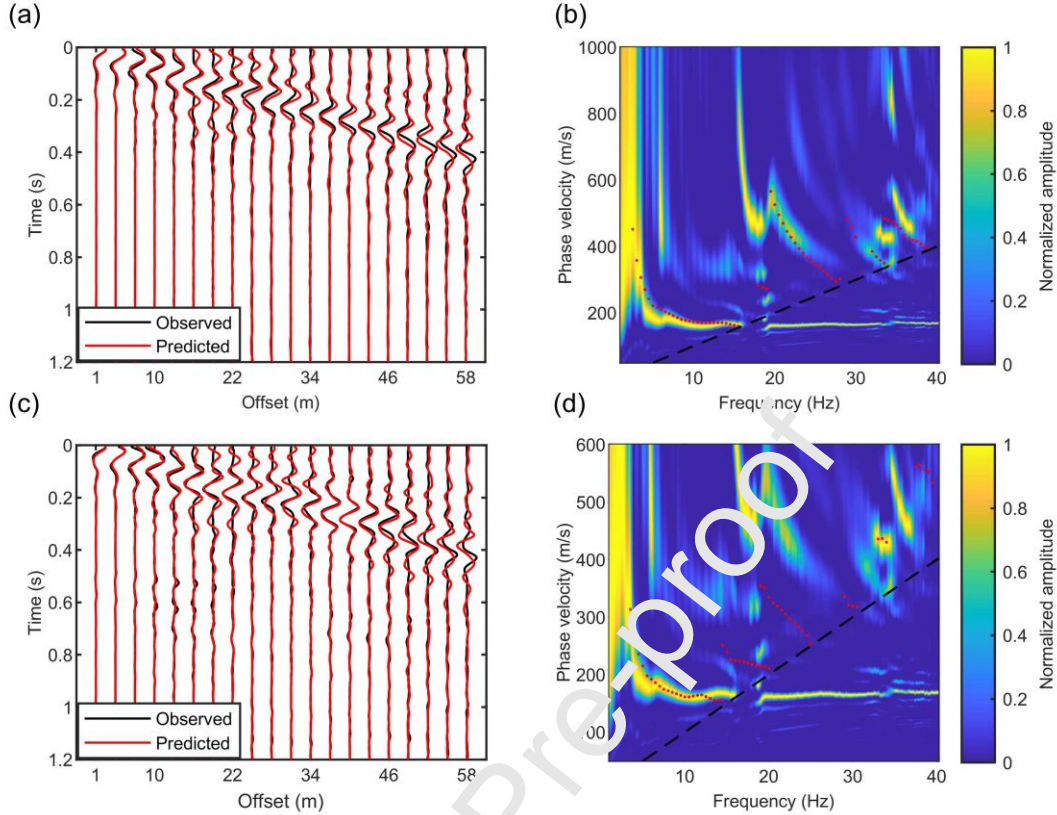


**Fig. 11.** The further credibility evaluation for the inversion results of the 8-th and 102-nd sub-window. The comparison (a) between the observed CCFs and predicted CCFs of the 8-th sub-window. The dispersion spectrum (b) of the predicted CCFs of the 8-th sub-window. (c) and (d) are the same exhibitions as (a) and (b), but for the 102-nd sub-window. For clarity, in (a) and (c), only the waveforms within 1.2 s with the channel-spacing at 3 m are shown, and the amplitude of each CCF is normalized to 0.5 according to the maximum absolute amplitude. The red dots in (b) and (d) denote the measured phase velocities of the corresponding sub-window, and the black dashed lines are defined by the gauge-length of the DAS data.

### 3.3. Geologic interpretation

After the second-stage inversion for all sub-windows, we adopt the kriging interpolation (jBuist, 2022) to merge all 1D  $V_s$  models to form the pseudo-2D S-wave velocity tomogram of

survey area. Finally, we use a similar Gaussian smoothing filter as Fu et al. (2022) to obtain the final pseudo-2D  $V_s$  model (Fig. 12). We also collect the shallow-surface geological overview of the survey area, as shown by Table 1. Existing geological materials indicate that the near-surface stratigraphy below the survey area is composed of lake-bed alluvium with a thickness of 18~25 m, and the soil types are silty sand, sand, clayey sand and silty gravel (nees@UCSB, 2014). The alluvium is gradually transformed into strongly weathered granite at the depth range from 18 m to 25 m, while the decomposed granite consisting of gravely sand exists at the depth interval 25~88 m (nees@UCSB, 2014). At 88 meters, the bedrock of the Southern California Peninsular Ranges, granodiorite, is reached (nees@UCSB, 2014). That is to say, the underground media of the survey area can be roughly divided into three formations, and it has been marked by the red dashed lines (Fig. 12). Furthermore, the pseudo-2D S-wave velocity profile is in good agreement with the known lithologic information (Table 1), and the possible fluctuations for the ancient lake-bed and basement are also revealed (Fig. 12). Moreover, the possible interlayer variations and isolated decomposed granite are also reflected in Fig. 12. This physical-reasonable S-wave velocity tomogram paints a bright picture of the utilization of DAS-derived multimodal surface-wave dispersion data.

**Table 1.** Shallow-surface geological overview of the survey area (nees@UCSB, 2014)

Layer no.	From (m)	To (m)	Formation and description
1	0	18~25	Lake-bed alluvium, strongly weathered granite at 18.0 ~25.0 m
2	25	88	Decomposed granite consisting of gravely sand
3	88	Deeper	The bedrock of the Southern California Peninsular Ranges, granodiorite



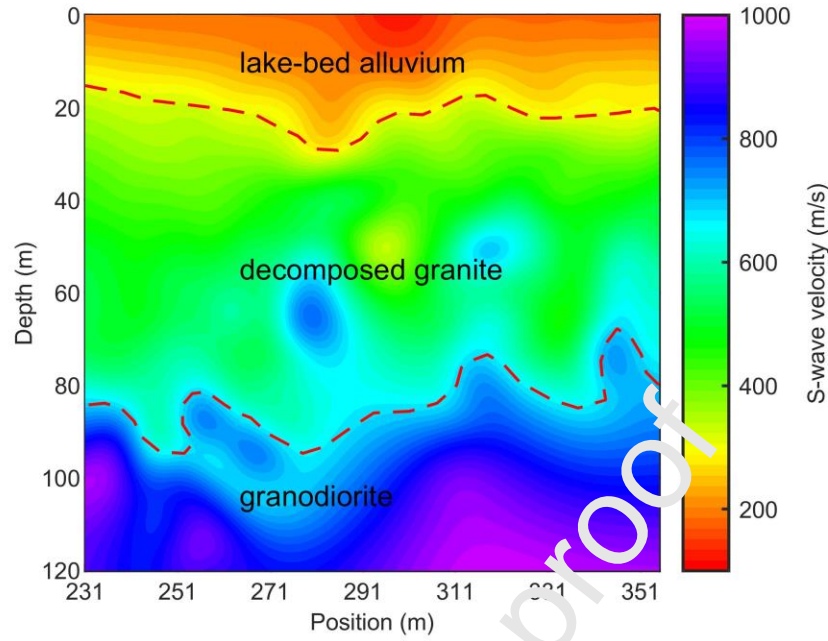


**Fig. 12.** The pseudo-2D S-wave velocity profile of the GVDA survey area. It is obtained by a Gaussian smoothing filter to the kriging interpolation (jBuist, 2022) result of all second-stage inversion results. The red dashed lines delineate the possible stratigraphic boundaries, and the words in the image describe the lithology of the corresponding formation.

#### 4. Conclusion

We take the DAS data of Long line I collected at Garner Valley Downhole Array survey area, California as a case, and adopt the inversion workflow of the multimodal surface wave dispersion curves consisting of staging strategy and PSEKM to exploit the subsurface S-wave velocity structure. The potential mode losses and aliasings in the dispersion observations can always be revealed by the second-stage inversion. The generated pseudo-2D S-wave velocity profile is in good agreement with the regional geological materials. In addition, we also compare different CCF stacking methods, and the PWS would give the better quality CCF, benefitting from this, the higher-mode surface waves dispersion measurement at the high frequency-band

would be achieved. We also analyze the role of the gauge-length for DAS system, indicating that the minimum wavelength can be measured reliably is also about one gauge-length in practice.

## Data Availability

The raw distributed-acoustic-sensing (DAS) data related to this article is available at <https://gdr.openei.org/submissions/481>, and the geological information about the Garner Valley Downhole Array (GVDA) test site can be accessed from <http://nees.ucsb.edu/facilities/GVDA>. The results in this paper are directly reproducible by downloading the code on GitHub (<https://github.com/wallacedos/SWPVPSEKMInv>).

## Declaration of Interest Statement

The authors declare that they have no known competing financial interests or personal relationships that could have appeared to influence the work reported in this paper.

## Credit Author Statement

**Yingwei Yan:** Conceptualization, Methodology, Software, Investigation, Writing - Original Draft, Writing - Review & Editing, Visualization. **Xiaofei Chen:** Formal analysis, Funding acquisition. **Jing Li:** Validation, Project administration. **Jianbo Guan:** Supervision. **Chaoqiang Xi:** Data Curation. **Hui Liu:** Resources.

## Acknowledgments

This work is supported by National Natural Science Foundation of China (Grant No. 41790465, U1901602, 42174065), Guangdong Provincial Key Laboratory of Geophysical High-resolution Imaging Technology (2022B1212010002), Shenzhen Key Laboratory of Deep Offshore Oil and Gas Exploration Technology (Grant No. ZDSYS20190902093007855), Shenzhen Science and Technology Program (Grant No. KQTD20170810111725321), and the

leading talents of Guangdong province program (Grant No.2016LJ06N652). This research is also supported by Natural Science Foundation of China (Grant No. 42222407).

## References

- Askari, R., Ferguson, R. J., Issac, J. H., Hejazi, S., 2015. Estimation of S-wave static corrections using CMP cross-correlation of surface waves. *J. Appl. Geophys.* 121, 42-53. <https://doi.org/10.1016/j.jappgeo.2015.07.004>
- Bensen, G. D., Ritzwoller, M. H., Barmin, M. P., Levshin, A. L., Lin, F., Moschetti, M. P., Shapiro, N. P., Yang, Y., 2007. Processing seismic ambient noise data to obtain reliable broad-band surface wave dispersion measurements. *Geophys. J. Int.* 169(3), 1239-1260. <https://doi.org/10.1111/j.1365-246X.2007.03374.x>
- Bouchon, M., 2003. A review of the discrete wavenumber method. *Pure. Appl. Geophys.* 160, 445-465. <https://doi.org/10.1007/PL00012545>
- Cheng, F., Chi, B., Lindsey, N.J., Daw, T.C., Ajo-Franklin, J.B., 2021. Utilizing distributed acoustic sensing and ocean bottom fiber optic cables for submarine structural characterization. *Sci Rep.* 11, 5613. <https://doi.org/10.1038/s41598-021-84845-y>
- Cheng, F., Lindsey, N. J., Souchevskaia, V., Dou, S., Freifeld, B., Wood, T., James, S. R., Wagner, A.M., Ajo-Franklin, J.B., 2022. Watching the cryosphere thaw: Seismic monitoring of permafrost degradation using distributed acoustic sensing during a controlled heating experiment. *Geophys. Res. Lett.* 49, e2021GL097195. <https://doi.org/10.1029/2021GL097195>
- Conn, A.R., Gould, N. I. M., Toint, P. L., 1991. A Globally Convergent Augmented Lagrangian Algorithm for Optimization with General Constraints and Simple Bounds. *SIAM. J. Numer. Anal.* 28(2), 545-572. <https://doi.org/10.1137/0728030>
- Dou, S., Lindsey, N., Wagner, A. M., Daley, T. M., Freifeld, B., Robertson, M., Peterson, J., Ulrich, C., Martin, E. R., Ajo-Franklin, J. B., 2017. Distributed Acoustic Sensing for Seismic Monitoring of the Near Surface: A Traffic-Noise Interferometry Case Study. *Sci. Rep.* 7, 11620. <https://doi.org/10.1038/s41598-017-11986-4>

Ernst, F. E., 2008. Multi-mode inversion for P-wave velocity and thick near-surface layers, Paper presented at Near Surface 2008 - 14<sup>th</sup> European Meeting of Environmental and Engineering Geophysics, Kraków, Poland. <https://doi.org/10.3997/2214-4609.20146236>

Fäh, D., Kind, F., Giardini, D., 2003. Inversion of local S-wave velocity structures from average H/V ratios, and their use for the estimation of site-effects. *Journal of Seismology*. 7, 449-467. <https://doi.org/10.1023/B:JOSE.00000005712.86058.42>

Fu, L., Pan, L., Li, Z., Dong, S., Ma, Q., Chen, X., 2022. Improved high-resolution 3D Vs model of Long Beach, CA: Inversion of multimodal dispersion curves from ambient noise of a dense array. *Geophys. Res. Lett.* 49, e2021GL097619. <https://doi.org/10.1029/2021GL097619>

Guan, J., Li, Y., Yan, Y., Yang, Z., Liu, G., 2022. Linear array analysis of passive surface waves combined with mini-Sosie technique. *Geophys. J. Int.* 230(3), 2131-2146. <https://doi.org/10.1093/gji/ggac169>

Guo, Z., Li, X., 2015. Rock physics model-based prediction of shear wave velocity in the Barnett Shale formation. *J. Geophys. Eng.* 12(3), 527-534. <https://doi.org/10.1088/1742-2132/12/3/527>

Haney, M. M., Nakahara, H., 2014. Surface-Wave Green's Tensors in the Near Field. *Bull. Seismol. Soc. Am.* 104(3), 1578-1586. <https://doi.org/10.1785/0120130113>

Imai, T., Tonouchi, K., 1982. Correlation of N value with S-Wave Velocity and shear Modulus. Paper presented at Proceedings of the Second European Symposium on Penetration Testing, Amsterdam, Netherlands.

jBuist, 2022. `kriging(x,y,z,range,sill)`. Retrieved from: MATLAB Central File Exchange. <https://www.mathworks.com/matlabcentral/fileexchange/57133-kriging-x-y-z-range-sill>

Jousset, P., Reinsch, T., Ryberg, T., Blanck, H., Clarke, A., Aghayev, R., Hersir, G. P., Henningses, J., Weber, M., Krawczyk, C. M., 2018. Dynamic strain determination using fibre-optic cables allows imaging of seismological and structural features. *Nat. Comm.* 9, 2509. <https://doi.org/10.1038/s41467-018-04860-y>

Kausel, E., 2018. Generalized stiffness matrix method for layer soils. *Soil. Dynam. Earthquake. Eng.* 115, 663-672. <https://doi.org/10.1016/j.soildyn.2018.09.003>

Kuhn, H. W., 1955. The Hungarian method for the assignment problem. *Nav. Res. Logist.* 2, 83-97. <https://doi.org/10.1002/nav.3800020109>

Lamuraglia, S., Stucchi, E., Aleardi, M., 2023. Application of a global–local full-waveform inversion of Rayleigh wave to estimate the near-surface shear wave velocity model. *Near Surface Geophysics*. 21(1), 21–38. <https://doi.org/10.1002/nsg.12243>

Lancelle, C.E., Baldwin, J. A., Lord, N., Fratta, D., Chalari, A., Wang, H. F., 2021. Using Distributed Acoustic Sensing (DAS) for Multichannel Analysis of Surface Waves (MASW). In *Distributed Acoustic Sensing in Geophysics* (eds Y. Li, M. Karrenbach and J.B. Ajo-Franklin). <https://doi.org/10.1002/9781119521808.ch16>

Liu, H., Li, J., Chi, B., 2022. Study of Distributed Acoustic Sensing Data Waveform Inversion Based on Strain Rate. *Chin. J. Geophys.* 65(9), 3584-3598. <https://doi.org/10.6038/cjg2022P0222>

Lord, N., Wang, H., Fratta, D., 2016. A source-synchronous filter for uncorrelated receiver traces from a swept-frequency seismic source. *Geophysics*. 81(5), P47–P55. <https://doi.org/10.1190/GEO2015-0324.1>

Luo, Y., Xia, J., Miller, R.D., Xu, Y., Liu, J., Liu, C., 2008. Rayleigh wave dispersive energy imaging using a high-resolution linear Radon transform. *Pure appl. Geophys.* 165(5), 903–922. <https://doi.org/10.1007/s00024-008-0338-4>

Maraschini, M., Ernst, F., Foti, S., Sacco, L. V., 2010a. A new misfit function for multimodal inversion of surface waves. *Geophysics* 75(4), G31–G43. <https://doi.org/10.1190/1.3436539>

Maraschini, M., Foti, S., 2010b. A Monte Carlo multimodal inversion of surface waves. *Geophys. J. Int.* 182(3), 1557-1566. <https://doi.org/10.1111/j.1365-246X.2010.04703.x>

Mari, J. L., 1981. Estimation of static corrections for shear-wave profiling using the dispersion properties of Love waves. *Geophysics*. 49(8), 1169–1179. <https://doi.org/10.1190/1.1441746>

McMechan, G.A. & Yedlin, M.J., 1981. Analysis of dispersive waves by wavefield transformation. *Geophysics*. 46(6), 869–874. <https://doi.org/10.1190/1.1441225>

Mosegaard, K., Tarantola, A., 1995. Monte Carlo sampling of solutions to inverse problems. *J. Geophys. Res.* 100(B7), 12431-12447. <https://doi.org/10.1029/94JB03097>

Munkres, J., 1957. Algorithms for the Assignment and Transportation Problems. *J. Soc. INDUST. Appl. MATH.* 5(1), 32-38. <https://doi.org/10.1137/0105003>

nees@UCSB., 2014. Garner valley downhole array. <http://nees.ucsb.edu/facilities/GVDA>

O' Neil, A., Matsuoka, T., 2005. Dominant Higher Surface-wave Modes and Possible Inversion Pitfalls. *J. Environ. Eng. Geophys.* 10(2), 185-201. <https://doi.org/10.2113/JEEG10.2.185>

Pan, L., Chen, X., Wang, J., Yang, Z., Zhang, D., 2019. Sensitivity analysis of dispersion curves of Rayleigh waves with fundamental and higher modes. *Geophys. J. Int.* 216(2), 1276-1303. <https://doi.org/10.1093/gji/ggy479>

Papadopoulou, M., Col, F. D., Mi, B., Bäckström, E., Marsden, P., Brodic, B., Malehmir, A., Socco, L. V., 2020. Surface-wave analysis for static corrections in mineral exploration: A case study from central Sweden. *Geophys. Prospect.* 68, 214-231. <https://doi.org/10.1111/1365-2478.12895>

Park, C.B., Miller, R.D., Xia, J., 1998. Imaging dispersion curves of surface waves on multi-channel record. *Proceedings of the SEG Technical Program Expanded Abstracts.* pp. 1377-1380. <https://doi.org/10.1190/1.1820161>.

Parker, T., Shatalin, S., Farhadiroushan, M., 2004. Distributed Acoustic Sensing-a new tool for seismic applications. *First Break.* 32(2), 61-69. <https://doi.org/10.3997/1365-2397.2013034>

Schimmel, M., Paulssen, H., 1997. Noise reduction and detection of weak, coherent signals through phase-weighted stacks. *Geophys. J. Int.* 130(2), 497-505. <https://doi.org/10.1111/j.1365-246X.1997.tb05664.x>.

Song, X., Li, D., Gu, H., Lin, Y., Ren, D., 2009. Insights into performance of pattern search algorithms for high-frequency surface wave analysis. *Comput. Geosci.* 35(8), 1603-1619. <https://doi.org/10.1016/j.cageo.2009.01.007>.

Socco, L. V., Ferraro, Boiero, D., 2010. Surface-wave analysis for building near-surface velocity models-established approaches and new perspectives. *Geophysics.* 75(5), 75A83-75A102. <https://doi.org/10.1190/1.3479491>

Song, Z., Zeng, X., Xu, S., Hu, J., Sun, T., Wang, B., 2020. Distributed Acoustic Sensing for imaging shallow structure I: active source survey. *Chin. J. Geophys.* 63(2), 532-540. <https://doi.org/10.6038/cjg2020N0184>

Song, Z., Zeng, X., Thurber, C. H., 2021. Surface-wave dispersion spectrum inversion method applied to Love and Rayleigh waves recorded by distributed acoustic sensing. *Geophysics.* 86(1), EN1-EN12. <https://doi.org/10.1190/GEO2019-0691.1>

Stokoe, K. H., Kurtulus, A., Menq, F.-Y., 2004. Data report: SASW measurements at the NEES Garner Valley test site, California, 13 January 2004. Retrieved from: <http://nees.ucsb.edu/sites/eot-dev.nees.ucsb.edu/files/facilities/docs/GarnerValley-SASWreport.pdf>.

Tan, C., Majid, T. A., Ariffin, K. S., Mohamad, N., 2012. Site-Specific Empirical Correlation between Shear Wave Velocity and Standard Penetration Resistance using MASW Method. IEEE Colloquium on Humanities, Science and Engineering (CHUSER), 94-97, <https://doi.org/10.1109/CHUSER.2012.6504288>

Uyanik, O., 2019. Estimation of the porosity of clay soils using seismic P- and S-wave Velocities. *J. Appl. Geophys.* 170, 103832. <https://doi.org/10.1016/j.jappgeo.2019.103832>

Vantassel, J. P., Cox, B. R., Hubbard, P. G., Yust, M., 2022. Extracting High-Resolution, Multi-Mode Surface Wave Dispersion Data from Distributed Acoustic Sensing Measurements using the Multichannel Analysis of Surface Waves. *J. Appl. Geophys.* 205, 104776. <https://doi.org/10.1016/j.jappgeo.2022.104776>

Wang, J., Wu, G., Chen, X., 2019. Frequency-Bessel transform method for effective imaging of higher-mode Rayleigh dispersion curves from ambient seismic noise data. *J. Geophys. Res.* 124(4), 3708-3723. <https://doi.org/10.1029/2018JB016595>

West, D. (2020). *Introduction to Graph Theory*, Second Edition (in Chinese). Beijing, China Machine Press.

Xia, J., Miller, R. D., Park, C. B., 1999. Estimation of near-surface shear-wave velocity by inversion of Rayleigh wave. *Geophysics*. 64(3) 691-700. <https://doi.org/10.1190/1.1444578>

Xia, J., Miller, R. D., Park, C. B., Tian, G., 2003. Inversion of high frequency surface waves with fundamental and higher modes. *J. Appl. Geophys.* 52(1), 45-57. [https://doi.org/10.1016/S0926-9851\(02\)00239-2](https://doi.org/10.1016/S0926-9851(02)00239-2)

Xia, J., Gao, L., Pan, Y., Shen, C., Yin, X., 2015. New findings in high-frequency surface wave method. *Chin. J. Geophys.* 58(8), 2591-2605. <https://doi.org/10.6038/cjg20150801>

Xi, C., Xia, J., Mi, B., Dai, T., Liu, Y., Ning, L., 2021. Modified frequency-Bessel transform method for dispersion imaging of Rayleigh waves from ambient seismic noise. *Geophys. J. Int.* 225(2), 1271-1280. <https://doi.org/10.1093/gji/ggab008>

Yan, Y., Chen, X., Huai, N., Guan, J., 2022a. Modern inversion workflow of the multimodal surface wave dispersion curves: staging strategy and Pattern search with embedded Kuhn-Munkres algorithm. *Geophys. J. Int.* 231(1), 47-71. <https://doi.org/10.1093/gji/ggac178>

Yan, Y., Li, J., Huai, N., Guan, J., Liu, H., 2022b. Two-station analysis of passive surface waves with continuous wavelet transform and plane-wave-based beamforming. *J. Appl. Geophys.* 197, 104526. <https://doi.org/10.1016/j.jappgeo.2021.104526>

Yilmaz, Ö., Eser, M., Berilgen, M., 2006. A case study of seismic zonation in municipal areas. *The Leading Edge*. 25(3), 319–330. <https://doi.org/10.1190/1.2184100>

Zeng, X., Lancelle, C., Thurber, C., Fratta, D., Wang, H., Lord, M., Chalari, A., Clarke, A., 2017. Properties of Noise Cross-Correlation Functions Obtained from a Distributed Acoustic Sensing Array at Garner Valley, California. *Bull. Seismol. Soc. Am.* 107(2), 603–610. <https://doi.org/10.1785/0120160168>

Zhang, K., Li, H., Wang, X., Wang, K., 2020. Retrieval of shallow S-wave velocity profiles from seismic reflection surveying and traffic-induced noise. *Geophysics*. 85(6), EN105-EN117. <https://doi.org/10.1190/geo2019-0845.1>

Zhou, J., Chen, X., 2021. Removal of Crossed Artifacts from Multimodal Dispersion Curves with Modified Frequency-Bessel Method. *Bull. Seismol. Soc. Am.* 112(1), 143-152. <https://doi.org/10.1785/0120210012>

Zywicki, D. J., Rix, G., I., 2005. Mitigation of the Near-Field Effects for Seismic Surface Wave Velocity Estimation with Cylindrical Beamformers. *Journal of Geotechnical and Geoenvironmental Engineering*. 131(8), 970-977. [https://doi.org/10.1061/\(ASCE\)1090-0241\(2005\)131:8\(970\)](https://doi.org/10.1061/(ASCE)1090-0241(2005)131:8(970))



Credit Author Statement

**Yingwei Yan:** Conceptualization, Methodology, Software, Investigation, Writing - Original Draft, Writing - Review & Editing, Visualization.

**Xiaofei Chen:** Formal analysis, Funding acquisition.

**Jing Li:** Validation, Project administration.

**Jianbo Guan:** Supervision.

**Chaoqiang Xi:** Data Curation.

**Hui Liu:** Resources.

#### Declaration of Interest Statement

The authors declare that they have no known competing financial interests or personal relationships that could have appeared to influence the work reported in this paper.

Journal Pre-proof

### Highlights

1. Propose the cylindrical-wave phase-shift for dispersion spectrum calculation.
2. Construct a dedicated workflow for DAS data analysis.
3. The inversion method without high-mode order-label is adopted.
4. Mode-losses and aliasings of dispersion curves are revealed by our method.